HHS Public Access

Author manuscript

Mater Sci Eng C Mater Biol Appl. Author manuscript; available in PMC 2017 November 01.

Published in final edited form as:

Mater Sci Eng C Mater Biol Appl. 2016 November 1; 68: 746–757. doi:10.1016/j.msec.2016.06.047.

Hydrothermally processed 1D hydroxyapatite: mechanism of formation and biocompatibility studies

Zoran S. Stojanović[1], **Nenad Ignjatović**[1], **Victoria Wu**[2], **Vojka Žunič**[3], **Ljiljana Veselinović**[1], **Srečo Škapin**[3], **Miroslav Miljković**[4], **Vuk Uskoković**[2,5], and **Dragan Uskoković**[1,*]

[1]Centre for Fine Particles Processing and Nanotechnologies, Institute of Technical Sciences of the Serbian Academy of Sciences and Arts, Knez Mihailova 35/4, 11000 Belgrade, Serbia

[2]Advanced Materials and Nanobiotechnology Laboratory, Department of Bioengineering, University of Illinois, 851 South Morgan Street, Chicago, IL 60607-7052, USA

[3]Advanced Materials Department, Joţef Stefan Institute, Jamova cesta 39, 1000 Ljubljana, Slovenia

[4]Laboratory for Electron Microscopy, Faculty of Medicine University of Niš, Dr. Zoran Đinđić Boulevard 81, 18 000 Niš, Serbia

[5]Department of Biomedical and Pharmaceutical Sciences, School of Pharmacy, Chapman University, 9401 Jeronimo Road, Irvine, CA 92618-1908, USA

Abstract

Recent developments in bone tissue engineering have led to an increased interest in one-dimensional (1D) hydroxyapatite (HA) nano- and micro-structures such as wires, ribbons and tubes. They have been proposed for use as cell substrates, reinforcing phases in composites and carriers for biologically active substances. Here we demonstrate the synthesis of 1D HA structures using an optimized, urea-assisted, high-yield hydrothermal batch process. The one-pot process, yielding HA structures composed of bundles of ribbons and wires, was typified by the simultaneous occurrence of a multitude of intermediate reactions, failing to meet the uniformity criteria over particle morphology and size. To overcome these issues, the preparation procedure was divided to two stages: dicalcium phosphate platelets synthesized in the first step were used as a precursor for the synthesis of 1D HA in the second stage. Despite the elongated particle morphologies, both the precursor and the final product exhibited excellent biocompatibility and caused no reduction of viability when tested against osteoblastic MC3T3-E1 cells in 2D culture up to the concentration of 2.6 mg/cm^2. X-ray powder diffraction combined with a range of electron microscopies and laser diffraction analyses was used to elucidate the formation mechanism and the microstructure of the final particles. The two-step synthesis involved a more direct transformation of DCP to 1D HA with the average diameter of 37 nm and the aspect ratio exceeding 100:1. The comparison of crystalline domain sizes along different crystallographic directions showed no signs

*Corresponding author: Prof Dr Dragan Uskoković, dragan.uskokovic@itn.sanu.ac.rs.

of significant anisotropy, while indicating that individual nanowires are ordered in bundles in the b crystallographic direction of the $P6_{3/m}$ space group of HA. Intermediate processes, e.g., dehydration of dicalcium phosphate, are critical for the formation of 1D HA alongside other key aspects of this phase transformation, it must be investigated in more detail in the continuous design of smart HA micro- and nano-structures with advanced therapeutic potentials.

Keywords

hydrothermal; nanowires; hydroxyapatite; biomedical; particle size distribution

1. Introduction

The most prospective biocomposites in bone tissue engineering are the combinations of (a) natural biopolymers as the macroporous matrix phase and (b) inorganic, organic or hybrid nano- and micro-structures as the reinforcement phase [1–5]. Being the natural bone mineral phase and being known for an array of properties that favor bone tissue regeneration, ranging from biocompatibility to osteoconductivity to non-immunogenicity, hydroxyapatite (HA) is the natural material of choice for the reinforcement phase of biocomposites, rivaled in response only by a handful of other biomaterials, such as bioactive glass [6], chitin [7], carbon/graphene-based nanostructures [8,9], and a few others. A special interest in bone tissue engineering has been directed to nanoparticulate and nanostructured HA with large surface–area–to–volume ratios [10]. Osteoconductivity of the material containing such nanostructures is directly dependent on their specific surface area [11], which also favors the high loading capacity with respect to various biologically active substances, given that adsorption presents the sole mechanism of drug loading when it comes to HA. One-dimensional HA nano- and micro-structures for potential biomedical applications, such as tubes [12,13], wires [14], rods [15–17], ribbons [18] and similar, morphological porous and hierarchically assembled 3D varieties, are especially good candidates to fulfill these two demands. The combined effects of nano- and micro-sized surfaces in 1D HA materials could not only be optimal for cell proliferation and osteogenic differentiation, but also beneficial for the expression of angiogenetic factors in stem cell differentiation [19]. The development of procedures for controlled synthesis of 1D HA nanostructures is mainly driven by this goal, especially since the recent progress in this field still does not entirely meet the criteria for effective control over size and shape.

The first goal of this study was to successfully synthesize uniform 1D HA structures, ranging from micro- and nano-wires to micro- and nano-tubes to more complex morphological varieties, using a hydrothermal batch process on the gram scale. The framework for the synthesis was adopted by studying the traditional hydrothermal and solvothermal methods for the synthesis of 1D HA structures such as whiskers, ribbons, platelets and tubes [18,20–24] and organic modifiers assisted HA synthesis methods [25–27]. A detailed structural characterization of different intermediates and products of the method developed herein was then used to clarify the mechanism of the formation of 1D structures. By examining previous studies concerning the mechanism of 1D HA formation, we have divided the initially developed one-pot procedure into two stages to achieve a better

control over the product properties. Finally, since uniaxial growth is often accompanied by the less favorable particle/cell interface, biological assays were conducted to assess the cytotoxicity and biocompatibility of the synthesized particles in an *in vitro* setting.

2. Experimental details

2.1. Preparation of HA samples by synthesis path I

Two synthesis paths were investigated and a two-liter Parr hydrothermal reactor was used in both of them (Fig. 1). The first path was a single-stage, so-called one-pot preparation method involving (a) the precipitation of calcium and phosphate ions into dicalcium phosphate dihydrate (DCPD, aka brushite) with the addition of urea, and (b) a subsequent hydrothermal treatment of the resulting slurry. More specifically, 400 ml 0.12 M calcium acetate solution in water ($Ca(CH_3COO)_2 \cdot H_2O$, M_w=158.17 g/mol, 99 %, Acros Organics, Belgium) was added slowly (100 ml/h) to 400 ml 0.1 M solution of ammonium phosphate monobasic ($NH_4H_2PO_4$, M_w=115.03 g/mol, > 98 %, VWR International, USA), under strong mixing. pH value of the suspension following the addition of calcium acetate was 4.5. After mixing, 200 ml 0.6 M urea ($(NH_2)_2CO$, Mw=60.06, 99 %, Centrohem, Serbia) was added tothe dispersion and no pH change was detected. The 2 L PTFE liner in which this suspension had been made was then placed into a 2 L stainless steel cylinder of a Parr hydrothermal reactor and sealed for the hydrothermal treatment. The synthesis parameters are summarized in Table 1. All syntheses were run at 120 °C and ~ 7 bar pressure without mixing. The varied parameters were Ca/P molar ratio (via reducing the Ca content), the hydrothermal reaction time, and polyvinylpyrrolidone (PVP, K30, M_w=40,000 Da, Fluka AG, Switzerland) addition.

2.2. Preparation of HA samples by synthesis path II

The second path was composed of two stages and was designed to achieve a better control of 1D HA structures and help us gain a better insight into the mechanism of 1D HA formation. The first stage included the preparation of a calcium oleate complex and the precipitation of dicalcium phosphate anhydrous (DCPA, aka monetite) platelets. This precursor was then dried (or used freshly prepared) and hydrothermally treated in the second stage.

More specifically, calcium oleate complex was formed by adding 200 ml 0.25 M water – ethanol (3:7) solution of sodium oleate ($CH_3(CH_2)_7CH=CH(CH_2)_7COONa$, M_w=304.44 g/mol, ≥ 82 % oleic acid content, Sigma – Aldrich, Germany) in 200 ml 0.125 M aqueous solution of calcium – nitrate ($Ca(NO_3)_2 \cdot 4H_2O$, M_w=236.15 g/mol, ≥ 98 %, Sigma – Aldrich, Germany). Precipitated calcium oleate, a white sticky substance, was separated by decanting the liquid phase and immediately transferred to a 300 ml flask containing 200 ml water – ethanol (≈ 1:1) solution of ammonium phosphate monobasic ($NH_4H_2PO_4$, M_w=115.03 g/mol, > 98 %, VWR International, USA). Ca/P molar ratio in this stage was set to 0.5. The flask was then heated and brought to boiling in reflux for 5 h total. The hydrothermal precursor for Samples 7 and 8 was prepared with the addition of N,N–dimethylformamide (DMF) ($HCON(CH_3)_2$, M_w=73.10 g/mol, ≥ 98 %, Reanal, Hungary) into the flask three hours into the boiling process. After the completion of the reaction and cooling, the liquid phase was decanted and the products were repeatedly washed with ethanol, centrifuged, and

left to dry at 60°C overnight. The dried products were placed into a PTFE liner and dispersed by mechanical mixing in 1 L of 0.12 M urea solution. The hydrothermal reaction was run at 120 °C and 7 bars for 96 h without mixing. The synthesis parameters used in the making of the DCPA precursor and in the subsequent hydrothermal treatment are summarized in Table 2.

After the synthesis, the products were collected from the bottom of the liner and washed with distilled water and centrifuged numerous times. The washing of the samples was finished at the point when pH of the supernatant was ~ 5.5. The products were then dried for 24 h in an oven at 60 °C. The amount of calcium used in both synthesis routes was the same, and the mass of the dried products (yield) in each hydrothermal batch was near the theoretically calculated relative to the calcium content, e.g., 4.5 g for Sample2.

2.3. Characterization of samples

The precursors and products were characterized using X–ray powder diffraction (XRD, Philips PW1050 diffractometer with CuK$\alpha_{1,2}$ radiation), a scanning electron microscope (SEM, JEOL JSM 5300), a field-emission SEM (FE – SEM, ULTRA plus, Carl Zeiss) equipped with an energy-dispersive spectrometer (EDS, Inca 400, Oxford Instruments), a transmission electron microscope (JEM-2100, JEOL Inc., Tokyo, Japan), operating at 200 kV and equipped with a slow-scan CCD camera ORIUS SC1000A (Gatan Ltd.), an optical microscope (B-500MET with Optikam Pro 5LT digital camera, Optika, Italy) and laser diffraction analyzer (LD, Mastersizer 2000, Malvern Instruments). The ethanol suspensions of dried precursors and samples used for optical imaging were sonicated for 2 min and deposited as droplets on slides. Aqueous or ethanol suspensions of dried samples were used for the LD analysis, depending on the dispersibility of precursors and samples.

FTIR spectra were recorded using the KBr pellet technique at the room temperature on a Nicolet FT-IR 5700 spectrometer (Thermo Electron Corporation, USA) over the 4000–500 cm^{-1} wave number range, with 2 cm^{-1} resolution. Mixtools software package in R programming language was used to fit XRD and particle size distribution data. The size distribution of elongated particles, 1D and 2D structures, analyzed by LD methods appeared as a mixture of Gaussian distributions [28,29], i.e. a multimodal distribution. The function normalmixEM (expectation maximization algorithm) was used to fit the mixtures of univariate normals. To check how good the fit was, the Kolmogorov – Smirnov test was performed using an R function ks.test. The sample code, results and cumulative distributions of experimental and fitted data for DCP platelets are given in the supplementary section. The distributions were fitted with 2 or 3 Gaussians. The average diameters and aspect ratios of the synthesized nanowires (n = 91) were determined as a part of the image analysis performed using ImageJ software (National Institutes of Health, Bethesda, MD).

2.4. Cytotoxicity tests

Mouse calvarial pre-osteoblastic cell line, MC3T3-E1 subclone 4, was purchased from American Tissue Culture Collection (*ATCC*, Rockville, MD) and cultured in Alpha Minimum Essential Medium (α-MEM; *Gibco*) supplemented with 10% fetal bovine serum (FBS, *Invitrogen*) and containing no ascorbic acid. The medium was replaced every 48 h,

and the cultures were incubated at 37 °C in a humidified atmosphere containing 5% CO_2. Every 7 days, the cells were detached from the surface of the 75 cm^2 cell culture flask (*Greiner Bio-One*) using 0.25 wt% trypsin/EDTA, washed, centrifuged (3000 rpm × 5 min), resuspended in 10 ml media and subcultured in 1:10 volume ratio. To determine if the nanoparticles exhibited cytotoxic effects, MC3T3-E1 cells were seeded at 5×10^5 cells/well in 24-well plates and differentiated into the osteoblastic lineage for 14 days with 100 μg/ml of ascorbic acid as the chemical differentiation agent dissolved in α-MEM and in the presence of either 1 or 5 mg/well of nanoparticles. Cell viability was determined after 14 days of incubation using the Vybrant MTT cell proliferation assay (*Molecular Probes*) and following the manufacturer's instructions. Absorbance was read at 570 nm on a UV/Vis spectrophotometric microplate reader (*BGM Labtech, FLUostar Omega*). To examine the interaction between cells and nanoparticles, immunohistochemistry staining was done after 7 days of differentiation in the presence of nanoparticles. The 5×10^5 cells/well were seeded on glass coverslips, washed with phosphate buffer saline (PBS), and fixed for 5 minutes in 4% paraformaldehyde. Cells were then washed with PBS and incubated with Alexa Fluor 568 Phalloidin (1:400) (*Molecular Probes*) and OsteoImage™ bone mineralization staining agent (*Lonza*) for 30 minutes. Cells were then washed 3 times with PBS and cell nuclei were counterstained using NucBlue fixed cell ReadyProbe reagent (*Molecular Probes*) for 20 minutes. Images were obtained using a Zeiss LSM 710 confocal microscope (UIC core imaging facility). All the samples were analyzed in triplicates.

3. Results and discussion

3.1 One pot synthesis of HA nanowires and plates bundles

Preparation of the right precursors is the first and often the most crucial segment of the hydrothermal synthesis of fine powders. Due to the wide window of chemical parameters available for control in this stage (salts, complexes, hydroxides, oxides, solvents, *et cetera*), various combinations thereof are possible, each leading to a potentially unique product of the hydrothermal process [30]. The preparation of the precursor calcium phosphate precipitates, schematized in Fig. 1(a), carried out in an acidic medium (pH ≈ 4.5) and at room temperature, in the first synthesis method led to the formation of dicalcium phosphate dehydrate (DCPD) [31,32], a white flaky precipitate, and could be represented with the following equation:

$$Ca^{2+}(aq) + H_2PO_4^-(aq) + 2H_2O \rightarrow CaHPO_4 \bullet 2H_2O \downarrow + H^+$$

With the molar ratio of Ca/P being ≥ 1 (Table 1), $H_2PO_4^-$ ions are expected to be fully consumed in the process, whereas the release of protons entailing the precipitation reaction leads to a drop in the pH, down to ~ 4.5. The concentration of OH^- ions, i.e. pH, is, in fact, critical for tuning the composition and morphology of calcium phosphates [32]. During the treatment, until its complete decomposition, urea provides a source for the steady release of OH^- ions and CO_2 at temperatures above 80 °C [21,33]. At the onset of the decomposition, OH^- ions are mostly neutralized by the free protons, which leads to the crystallization of either DCPD or anhydrous dicalcium phosphate (DCPA), depending on the temperature used [32,34]. Regardless of the chemical composition, crystal hydrates form at lower

temperatures compared to their anhydrous allotropes. This is the result of the large energy barrier associated with the dehydration process. DCPD, consequently, forms at lower temperatures, e.g. 50 °C and pH 5, and has a feathery appearance [32]. In contrast, DCPA and DCPD/DCPA mixtures form at higher temperatures and with different morphologies, typically appearing in form of thicker, micrometric plates [34,35]. The formation of DCPA via dehydration in the hydrothermal solution can be represented as:

$$\mathrm{CaHPO_4 \bullet 2H_2O} \xrightarrow{\Delta} \mathrm{CaHPO_4 + 2\,H_2O}$$

Upon the complete consumption of protons from the solution, the concentration of OH^- ions starts to gradually increase and their reaction with DCPD starts, yielding water in the conversion process. Eventually, if prolonged enough, subjugation to the attack of OH^- ions leads to the dissolution of DCP and recrystallization of HA via a dissolution–recrystallization mechanism representable by the following equations:

$$\mathrm{CaHPO_4 \bullet 2H_2O\,(s) + OH^- \rightarrow Ca^{2+}\,(aq) + PO_4{}^{3-}\,(aq) + 3H_2O}$$
$$\text{and/or}$$
$$\mathrm{CaHPO_4\,(s) + OH^- \rightarrow Ca^{2+}\,(aq) + PO_4{}^{3-}\,(aq) + H_2O}$$

The formation of HA can occur either subsequently, following the dissolution of DCP, or simultaneously, depending on the kinetic conditions under which urea decomposes:

$$\mathrm{5\,Ca^{2+}\,(aq) + 3\,PO_4{}^{3-}\,(aq) + OH^-\,(aq) \rightarrow Ca_5(PO_4)_3OH\downarrow}$$

Results of the XRD phase analysis of samples synthesized by following the single-stage, “one pot” route are shown in Fig. 2(a, b). All the reflections in the XRD patterns match those of the HA reference (AMCSD 0009357) [31]. The comparison of crystalline domain sizes calculated along different crystallographic directions using Scherrer’s equation (Appendix A: Supplementary data, Table A1) shows no signs of significant anisotropy of scattering domains.

The highest ratio of crystallite sizes, 3.23, corresponding to reflections (002) and (121), was observed in Sample 2, which consisted of highly elongated particles wrapped up in bundles (Figs. 3(a) and A1). However, samples denoted as 1, 3 and 4, consisting of bundles of thin HA plates (Fig. 3(b), A2(a, b, c), and A3(a, b)), display nearly identical crystallite sizes for mutually perpendicular, (002) and (300) reflections. For other samples synthesized using the same, “one pot” method, Samples 2 and 5, this ratio was around 2, the reason being lower crystallite sizes in the (300) direction in comparison to Samples 1, 3 and 4. This leads to the conclusion that crystallites forming bundles in Samples 1, 3 and 4, synthesized at the lowest reaction time (20 h), are ordered in the *b* crystallographic direction. By increasing the reaction time to 48 h or 96 h, the bundles disintegrate and 1D HA forms appear, as observed for Samples 2 and 5 (Fig. 3(b) and (e); Figs. A1, A2(d) and A3(c)). A considerably lower crystallite size than the longest particle dimensions also confirms the polycrystalline nature of 1D HA and validates the aggregational growth model now presumed to apply to all forms

of HA, be they biological or synthetic. LD particle size distribution parameters, including the volumetric mixing proportion (λ), the component median (μ) and the standard deviation (σ), are shown in Figs. 3 and A3 for all five samples synthesized using the “one pot” method. The difference in the mixing proportion of a component with the smallest median diameter (blue color) indicates that the bundles of platelets disintegrate at longer reaction times. Only a small fraction of loose particles was detected in Samples 1, 3, and 4, this may be due to edges and corrugations on bundled plates rather than to loose particles *per se*. This can explain the difference in μ-s and σ-s of the smallest particle component in these five samples.

The formation of plate-like HA structures and their bundles observed in almost all of the Samples1 – 5 could not be explained by the dissolution–recrystallization mechanism onlybecause the latter would result in hexagonal, far more uniaxially grown structures that those evidenced in this case. The crystallization of plate-shaped HA structures thus requires the presence of octacalciumphosphate (OCP) as an intermediate phase. OCP has a layered structure composed of alternating apatitic and hydrated layers [36–38]. The layered OCP has a thin, plate-likemorphology, often resembling ribbons or blades, in contrast to hexagonal HA microcrystals, which are usually of needle-shaped character. Yet, the crystal structure of the apatitic layers in OCP and HA is remarkably similar [39–43]. The conversion of DCP to HAp via OCP can be represented by the following equations:

$$8\,\mathrm{CaHPO_4 \bullet H_2O} + 3\mathrm{H_2O} \rightarrow \mathrm{Ca_8(HPO_4)_2(PO_4)_4 \bullet 5H_2O} + 2\,\mathrm{H_3PO_4}$$

$$\mathrm{Ca_8(HPO_4)_2(PO_4)_4 \bullet 5H_2O} + 3\mathrm{OH^-} + 2\,\mathrm{Ca^{2+}(aq)} \rightarrow \mathrm{Ca_{10}(PO_4)_6(OH)_2} + \mathrm{H^+} + 6\mathrm{H_2O}$$

Intermediately, hydroxyl groups react with hydrogen phosphates within hydrated OCP layers to yield phosphates incorporable into the apatite lattice:

$$\mathrm{HPO_4^{2-}} + \mathrm{OH^-} \rightarrow \mathrm{PO_4^{3-}} + \mathrm{H_2O}$$

In contrast to the dissolution – recrystallization mechanism, here we have a solid-to-solid conversion. The result is HA of the characteristic morphology, explaining along the way the evolution of delaminated structures observed in all the samples prepared using the “one pot” method, especially Samples 1, 3 and 4. The variation of Ca/P ratio and the addition of PVP in the ranges and amounts tested in this study (Table 1) had no effects on the morphology. The choice of PVP was justified by its prior association with the uniaxial growth of HA crystals [44]. The diffractograms and optical micrographs of the one–pot precursor of Samples 1 and 2 are shown in Fig. 2(a, b) and Fig. A6(a), respectively. The precursor is identified as DCPD (brushite) and exhibits an irregular plate-like morphology. The obvious change in the morphology *en route* from the precursors to the products in the one-pot synthesis indicates that the dominant formation mechanism is dissolution – recrystallization. Still, solid state conversion could not be excluded as a mechanism of formation of irregular plate–like particles in Samples 1 – 5.

The complexity of the transformation mechanisms observed in this system and its relative insusceptibility to morphological control called for a more simplistic approach in the

synthesis of the desired, 1D morphological structures. The partitioning of synthesis stages came out as one of the solutions.

3.2 Two stage synthesis of HA nanowires via DCPA precursor

The first step of this modified, two-stage synthesis procedure (Fig. 1(b)) belongs to the synthesis of DCPA precursors via hydrolysis of calcium oleate in a water–ethanol solution. Ethanol is used to increase the solubility of calcium oleate, a compound fairly soluble in hot ethanol, but practically insoluble in water. The precipitation of DCPA can be described in this case with the following reactions:

$$\mathrm{H_2PO_4^- \leftrightarrow H^+ + HPO_4^{2-}}$$
$$\mathrm{Ca(OL)_2 + 2H^+ \leftrightarrow Ca^{2+} + 2OLH}$$
$$\mathrm{Ca^{2+} + HPO_4^{2-} + 2H_2O \rightarrow CaHPO_4 \bullet 2H_2O \downarrow}$$
$$\mathrm{CaHPO_4 \bullet 2H_2O \xrightarrow{\Delta} CaHPO_4 + 2\,H_2O}$$

where OL^- is the oleate anion, $CH_3(CH_2)_7CH{=}CH(CH_2)_7COO^-$, and OLH is the oleic acid, a product of the hydrolysis reaction.

Figure 4 shows XRD patterns of the precursor powders following drying in an oven at 60 °C for one day. Interestingly, all powders converted to HA, demonstrating the transient stability of DCPA. Micrographs of the precursor powders shown in Fig. 5, most importantly, show the lamination of platelets. All the precursor samples contained platelets with a lamellar substructure, being the results of the specific growth habit typical for DCPA crystals. Then, the (−1 2 0) reflection in the precursor for Sample 7, prepared with the addition of DMF, is distinctively more intense than the one in the precursor for Sample 6, prepared using the same parameters but excluding DMF. Sample 7 was also synthesized using different precursor concentrations so as to investigate the previously suggested influence of DMF on crystallization of calcium phosphates [35] and is shown as supplementary data. The mechanism for this effect has not been elucidated yet, but has been exploited in “one pot” solvothermal syntheses of different 1D and 2D forms of HA [35]. Although the use of DMF does induce a structural change in synthesized DCPA, all of the precursors synthesized in its presence had the same morphology (Fig. A4). Another effect that plays a crucial role in ensuring the growth of regularly shaped platelets comes from oleic complexes as Ca^{2+}concentration buffers as well as of oleic anions as agents for the directed, face-specific growth. Namely, as the oleic anion, OL^-, tends to form a complex bond with Ca^{2+}, crystal planes terminated with the largest density of Ca^{2+} ions will tend to exhibit the largest inhibition of growth.

Dried precursors were used for the synthesis of HA Samples 6 and 7, while Sample 8 was hydrothermally synthesized using a freshly made and washed, but not dried, precursor otherwise identical to that of Sample 7. The difference in the crystallite size between these samples, as shown in Table A1, was insignificant. All the samples were identified as HA, with only a slight difference in the diffraction peak intensity ratios (Fig. 6).

Morphologically, however, the samples were very different, as seen from the corresponding SEM images (Fig. A5). Thus, Sample 6 consists of fine needle–like particles, oftentimes

arranged in ladders or woven platelets (Figs. 7 and A5(a)). Sample 7 consists of long wires with up to 10 μm in length and around 30 nm in diameter, having the aspect ratio of over 100:1 (Fig. 8). The morphology of particles comprising Sample 8 is slightly different from those found in Sample 6. It is characterized by a small extent of disintegration, the result of which are particles with retained plate-like morphology, but with brush-like ends (Fig. A5 (c)).

Morphological changes associated with the transformation of DCPA to HA were observed and discussed in the literature. The predominant transformation, accompanying the dehydration of DCPD, is thought to involve the formation of splinters, which then transition to nanorods and nanofibers, transforming along the way to HA [23,35], though the one involving OCP as the intermediate phase appears to be equally prominent [47]. Both mechanisms assume that the preserved morphology of the precursor is due to the similarity of the crystal structures of DCPA and OCP to HA. Again, ribbon–like morphologies are typically attributable to the transformation via OCP, whereas DCPA tends to dissolve and form splinters which regrow into elongated 1D shapes and eventually rearrange into hierarchically ordered structures. In this study we have come up with a clear evidence of the effect that the structural changes of DCPA precursors have on the morphology of the resulting HA particles. Under all the conditions tested for the hydrothermal transformation of DCPA into 1D HA structures, the complete conversion of shapes occurredin one case only (Sample 7).

The mechanism for the formation of uniform 1D HA structures is dissolution/ recrystallization, kinetically limited and controlled by the gradual solubility of DCPA as the intermediate and the source of ions for the growth HA. Whereas abrupt increases in supersaturation favor the formation of rounded and smaller particles, slow increases in supersaturation favor the elongation of HA crystals, alongside excluding the epitaxial growth of HA on an OCP template in the form of plates [21]. Urea decomposition is one factor enabling the slow release of a constitutive ion, OH^-, and its concentration can be tuned by controlling the temperature of the hydrothermal treatment, i.e. temperature at which urea decomposes. Another factor, equally critical, is the intermediate dissolution of DCPA. For example, if the surface of DCP is blocked with oleic species, the dissolution is hindered and non-uniform growth results. The precise coupling of the two simultaneously occurring processes - dissolution/recrystalization and solid–to–solid conversion – appears to be crucial in order to obtain elongated and uniform morphologies. The presence of OCP, that occurs as an intermediary in the one-pot synthesis, can be used as an indicator that the transformation of DCP to HA is not direct enough and not optimized to yield 1D structures. Thus we believe that controlling the concentration of OH^- ions throughout the growth process in a specific, relatively narrow range is a key factor in favor of the growth of 1D structures. It can be tuned by controlling the temperature of the hydrothermal process (mainly in lower and mild temperature ranges) and the amount of urea as the source of OH^- ions.

3.3 FTIR analysis of precursors and samples

The FTIR spectra of the DCPD precursor for Samples 1 and 2, of Ca oleate complex, and of the DCPA precursors for Samples 6 – 8, along with the corresponding final products, are

shown in Fig. 9. Based on the FTIR spectrum of the one-pot synthesis precursor, Fig. 9(a), it is identified as pure DCPD [48,49] (purple line). The spectra of precursors used in the second, two-stage synthetic approach (Samples 6 – 8) are identified as DCPA (green and black lines) and are shown along with the IR spectrum of calcium oleate complex (blue line). The prominent bands at 2923 cm^{-1} and 2852 cm^{-1} correspond to the asymmetric and symmetric stretch of -CH_2- groups. The characteristic doublet at 1577 cm^{-1} and 1541 cm^{-1}, together with the bands at 1467 cm^{-1} and 1429 cm^{-1}, is assigned to the asymmetric and symmetric stretch of -COO^- groups [50,51]. The given bands are characteristic for calcium oleate (calcium dioleate) complex. The DCPA precursors have characteristic bands originating from P-O- and P-O-H bonds at 1131 cm^{-1}, 1067 cm^{-1}, 902 cm^{-1}, 578 cm^{-1} and 530 cm^{-1}. The band at 1637 cm^{-1} results from the H-O-H bending and rotation of the residual water, while bands at 2923 cm^{-1} and 2852 cm^{-1} are attributed to –CH_2– groups from oleate anions adsorbed on the surface of monetite. Distinct bands arise in the precursor of Sample 6, specifically at 1707 cm^{-1} and 1736 cm^{-1}, corresponding to adsorbed oleic acid dimer and monomer, respectively [52]. This specific band does not exist in the spectrum of the precursor for Samples 7 and 8. This might be the effect of hydrolysis of oleate at lower pH values during the reaction to which DMF is not added. The addition of DMF raises pH of the reaction medium and prevents the hydrolysis of oleate anion and its conversion to oleic acid [53]. FTIR spectra of HA samples contain all four characteristic apatite phosphate vibration modes with bands at 1094 cm^{-1}, 1031 cm^{-1}, 961 cm^{-1}, 602 cm^{-1} and 564 cm^{-1} [54].

From these characterization data, we can conclude that two key factors play a role in determining the final morphology of HA samples synthesized using the two-stage method. The first is the adsorption of oleic species and the second is the drying of the freshly synthesized precursor. In the case of the adsorption of oleic acid, presumably in bilayers, as we assume it occurs on the DMF-free precursor of Sample 6, it must entail a significant change of surface hydrophilicity. Specifically, the surface becomes more hydrophobic, which slows down the kinetics of dissolution. Sample 6 is morphologically different from Sample 8, in a way that platelets appear more disintegrated, albeit not fully. Dissolution was more intense than in Sample 8, but less than in Sample 7. The formation of HA nanowires observed in all three samples can be attributed to the presence of oleate ion, which is capable of binding more intensely to Ca^{2+} on the surface of HA;this would explain the more directed and uniaxial growth of HA. As for the second effect, the drying of the precursor, we believe that low temperature transformation, physical or chemical, may occur, e.g., dehydration of DCPD to DCPA and/or desorption of oleate species. One must notice that the characterized precursors were dried at 60 °C for 24 h. Sample 8 is prepared using a freshly synthesized precursor without the drying step during which we believe the solid–to–solid chemical reaction is promoted; as a result, the plate-like morphology is being predominantly retained. These intermediate processes, alongside other key aspects of this phase transformation, must be investigated in more detail in the design of HA micro- and nano-structures with advanced therapeutic potentials.

3.4 In vitro study of synthesized DCPA platelets and HA nanowires

Cytotoxicity and biocompatibility of DCPA platelets as precursorsfor HA nanowires comprising Sample 7, as well as of the given HA nanowires, were examined *in vitro*, in osteoblastic MC3T3-E1 cell culture. The MTT assay measures the mitochondrial succinic dehydrogenase activity and is a strong indicator of cytotoxic effects affecting cell viability. Elongated particle morphologies are often associated with increased cytotoxicity, even for compositions for which round particle shapes have no adverse effects on cells. Although tremolite [55] and other asbestoses [56] are paradigmatic examples in favor of this effect, the latter has been observed for multiple other particle compositions, ranging from titania [57] to carbon nanotubes [58] to ceria [59]. Moreover, compared to spherical HA nanoparticles, needle-shaped ones induced a considerably higher cytotoxicity and inflammatory cytokines production in BEAS-2B and RAW264.7 cells than the spherical ones [60]. Apoptosis mediated by a mitochondrial-dependent pathway in primary rat osteoblasts was also noticeably increased following incubation with needle-shaped HA particles as opposed to the spherical ones [61]. Such apoptotic effects observedin HepG2 cells were the basis for proposing HA as utilizable in the treatment of hepatoma and other types of cancer [62]. Needle-shaped HA also slowed down the cell metabolism and inhibited hatching in catfish T-cells and zebrafish embryos in a dose-dependent manner [63]. Other studies suggested good biocompatibility and a lack of cytotoxic effects of needle-shaped HA when tested *in vitro* [64,65], demonstrating a great degree of variability of the biological response to such morphologies. The exact amount, shape, texture, aspect ratio, surface charge, agglomeration degree, the dosage mode (seeding cells onto the powder, depositing powder on top of the cells or co-seeding), the cell type and the interaction of the particles with biomolecules contained in the growth medium are all factors influencing the biological response to them, needing further studies to be discerned and analyzed. As seen in Fig. 10, no decrease in cell viability was observed for any of the three calcium phosphate samples (spherical HA standard, needle-shaped HA comprising Sample 7, and DCPA as the precursor for Sample 7) in comparison with the particle-free control. The only significant difference in viability was observed for the spherical HA nanoparticle standard synthesized using a previously reported protocol [66]: cells incubated with this powder demonstrated a higher viability compared to the control, particle-free cell population, albeit only at the lower of the two tested particle concentrations (Fig. 10). Also, the elongated HA particles comprising Sample 7 did not cause any significant change in cell viability compared to the spherical HA nanoparticle standard at either of the two particle concentrations. These results corroborate our previous finding of no markedly negative effects on osteoblastic cells exerted by elongated particles of DCPA synthesized in an urea-assisted precipitation process except for the mild granulations of the cytoskeletal microfilaments [67]. In spite of the dosage amount exceeding fifty times that for which apoptotic effects were observed in osteoblasts in an earlier study [61] (0.02 – 1 vs. 1 – 5 mg/ml), no inhibitory effects or cellular injury were detected for 1D HA fabricated in this study.

Concordantly, immunofluorescent images shown in Fig. 11 demonstrate a favorable particle/cell interface for both the DCPA precursor and the final product, HA, of Sample 7. Cytoskeletal f-actin microfilaments display a continuous, uninterrupted structure, devoid of aggregations, signifying a healthy internal structure and morphology of the cells in contact

with the particles. No difference between the control, particle-free cell populations and those incubated with these two types of elongated particles of calcium phosphate was observed.

4. Conclusion

In summary, we designed a two-stage process for the high-yield synthesis of 1D HA nanostructures with diameters on the nano scale and aspect ratios exceeding 100:1. Optimization of the DCP precursor for the hydrothermal synthesis is required for its transformation to 1D HA to reach completion. To achieve a better control over particle size and morphology, the first stage of the process, involving the synthesis of DCP, must be investigated in more detail. Understanding the effect of various hydrothermal processing parameters, to which this study has contributed, will help in gaining a better control over this process and making it more suitable for the application as a method for the high-yield synthesis of various other 1D HA micro- and nano-structures. *In vitro* studies on osteoblastic cells demonstrated the absence of any cytotoxic effects caused by the particles and a very high level of biocompatibility, indicating a pronouncedly promising potential of these HA systems for biomedical applications.

Supplementary Material

Refer to Web version on PubMed Central for supplementary material.

Acknowledgments

The Ministry of Education, Science and Technological Development of the Republic of Serbia grant III45004 and National Institute of Health grant R00-DE021416 are acknowledged for support.

References

1. Roeder RK, Converse GL, Kane RJ, Yue W. Hydroxyapatite-reinforced polymer biocomposites for synthetic bone substitutes. JOM. 2008; 60:38–45.
2. Aston DE, Bow JR, Gangadean DN. Mechanical properties of selected nanostructured materials and complex bio-nano, hybrid and hierarchical systems. Int Mater Rev. 2013; 58:167–202. DOI: 10.1179/1743280412Y.0000000012
3. Fang Z, Feng Q. Improved mechanical properties of hydroxyapatite whisker-reinforced poly(l-lactic acid) scaffold by surface modification of hydroxyapatite. Mater Sci Eng C. 2014; 35:190–194. DOI: 10.1016/j.msec.2013.11.008
4. Munarin F, Petrini P, Gentilini R, Pillai RS, Dirè S, Tanzi MC, Sglavo VM. Micro- and nano-hydroxyapatite as active reinforcement for soft biocomposites. Int J Biol Macromol. 2015; 72:199–209. DOI: 10.1016/j.ijbiomac.2014.07.050 [PubMed: 25109458]
5. Uskoković V, Uskoković DP. Nanosized hydroxyapatite and other calcium phosphates: Chemistry of formation and application as drug and gene delivery agents. J Biomed Mater Res B Appl Biomater. 2011; 96B:152–191. DOI: 10.1002/jbm.b.31746 [PubMed: 21061364]
6. Liu T, Ding X, Lai D, Chen Y, Zhang R, Chen J, Feng X, Chen X, Yang X, Zhao R, Chen K, Kong X. Enhancing in vitro bioactivity and in vivo osteogenesis of organic–inorganic nanofibrous biocomposites with novel bioceramics. J Mater Chem B. 2014; 2:6293.doi: 10.1039/C4TB00889H
7. Li X, Yang Y, Fan Y, Feng Q, Cui F, Watari F. Biocomposites reinforced by fibers or tubes as scaffolds for tissue engineering or regenerative medicine: Biocomposites Reinforced by Fibers or Tubes. J Biomed Mater Res A. 2014; 102:1580–1594. DOI: 10.1002/jbm.a.34801 [PubMed: 23681610]

8. Wan C, Chen B. Poly(ε-caprolactone)/graphene oxide biocomposites: mechanical properties and bioactivity. Biomed Mater. 2011; 6:055010.doi: 10.1088/1748-6041/6/5/055010 [PubMed: 21921319]
9. Liao CZ, Li K, Wong HM, Tong WY, Yeung KWK, Tjong SC. Novel polypropylene biocomposites reinforced with carbon nanotubes and hydroxyapatite nanorods for bone replacements. Mater Sci Eng C. 2013; 33:1380–1388. DOI: 10.1016/j.msec.2012.12.039
10. Wang P, Zhao L, Liu J, Weir MD, Zhou X, Xu HHK. Bone tissue engineering via nanostructured calcium phosphate biomaterials and stem cells. Bone Res. 2014; 2:14017.doi: 10.1038/boneres.2014.17 [PubMed: 26273526]
11. Lee DSH, Pai Y, Chang S, Kim DH. Microstructure, physical properties, and bone regeneration effect of the nano-sized β-tricalcium phosphate granules. Mater Sci Eng C. 2016; 58:971–976. DOI: 10.1016/j.msec.2015.09.047
12. Chandanshive BB, Rai P, Rossi AL, Ersen O, Khushalani D. Synthesis of hydroxyapatite nanotubes for biomedical applications. Mater Sci Eng C. 2013; 33:2981–2986. DOI: 10.1016/j.msec.2013.03.022
13. Sun Q, Lou JT, Kang F, Chen JF, Wang JX. Facile preparation of hydroxyapatite nanotubes assisted by needle-like calcium carbonate. Powder Technol. 2014; 261:49–54. DOI: 10.1016/j.powtec.2014.04.014
14. Costa DO, Dixon SJ, Rizkalla AS. One- and Three-Dimensional Growth of Hydroxyapatite Nanowires during Sol–Gel–Hydrothermal Synthesis. ACS Appl Mater Interfaces. 2012; 4:1490–1499. DOI: 10.1021/am201735k [PubMed: 22296410]
15. Deng Y, Wang H, Zhang L, Li Y, Wei S. In situ synthesis and in vitro biocompatibility of needle-like nano-hydroxyapatite in agar–gelatin co-hydrogel. Mater Lett. 2013; 104:8–12. DOI: 10.1016/j.matlet.2013.03.145
16. Peng F, Yu X, Wei M. In vitro cell performance on hydroxyapatite particles/poly(l-lactic acid) nanofibrous scaffolds with an excellent particle along nanofiber orientation. Acta Biomater. 2011; 7:2585–2592. DOI: 10.1016/j.actbio.2011.02.021 [PubMed: 21333762]
17. Jevtić M, Mitrić M, Škapin S, Jančar B, Ignjatović N, Uskoković D. Crystal Structure of Hydroxyapatite Nanorods Synthesized by Sonochemical Homogeneous Precipitation. Cryst Growth Des. 2008; 8:2217–2222. DOI: 10.1021/cg7007304
18. Zhang Y, Lu J, Wang J, Yang S, Chen Y. Synthesis of nanorod and needle-like hydroxyapatite crystal and role of pH adjustment. J Cryst Growth. 2009; 311:4740–4746. DOI: 10.1016/j.jcrysgro.2009.09.018
19. Xia L, Lin K, Jiang X, Fang B, Xu Y, Liu J, Zeng D, Zhang M, Zhang X, Chang J, Zhang Z. Effect of nano-structured bioceramic surface on osteogenic differentiation of adipose derived stem cells. Biomaterials. 2014; 35:8514–8527. DOI: 10.1016/j.biomaterials.2014.06.028 [PubMed: 25002263]
20. Ma MG, Zhu YJ, Chang J. Monetite Formed in Mixed Solvents of Water and Ethylene Glycol and Its Transformation to Hydroxyapatite. J Phys Chem B. 2006; 110:14226–14230. DOI: 10.1021/jp061738r [PubMed: 16854124]
21. Neira IS, Kolen'ko YV, Lebedev OI, Van Tendeloo G, Gupta HS, Guitián F, Yoshimura M. An effective morphology control of hydroxyapatite crystals via hydrothermal synthesis. Cryst Growth Des. 2008; 9:466–474.
22. Jokić B, Mitrić M, Radmilović V, Drmanić S, Petrović R, Janaćković D. Synthesis and characterization of monetite and hydroxyapatite whiskers obtained by a hydrothermal method. Ceram Int. 2011; 37:167–173. DOI: 10.1016/j.ceramint.2010.08.032
23. Guo X, Yu L, Chen L, Zhang H, Peng L, Guo X, Ding W. Organoamine-assisted biomimetic synthesis of faceted hexagonal hydroxyapatite nanotubes with prominent stimulation activity for osteoblast proliferation. J Mater Chem B. 2014; 2:1760.doi: 10.1039/c3tb21652g
24. Lu BQ, Zhu YJ, Chen F, Qi C, Zhao XY, Zhao J. Solvothermal Transformation of Calcium Oleate Precursor into Large-Sized Highly Ordered Arrays of Ultralong Hydroxyapatite Microtubes. Chem - Eur J. 2014; :1–7. DOI: 10.1002/chem.201400252

25. Mohandes F, Salavati-Niasari M, Fereshteh Z, Fathi M. Novel preparation of hydroxyapatite nanoparticles and nanorods with the aid of complexing agents. Ceram Int. 2014; 40:12227–12233. DOI: 10.1016/j.ceramint.2014.04.066
26. Mohandes F, Salavati-Niasari M. Simple morphology-controlled fabrication of hydroxyapatite nanostructures with the aid of new organic modifiers. Chem Eng J. 2014; 252:173–184. DOI: 10.1016/j.cej.2014.05.026
27. Mohandes F, Salavati-Niasari M. Particle size and shape modification of hydroxyapatite nanostructures synthesized via a complexing agent-assisted route. Mater Sci Eng C. 2014; 40:288–298. DOI: 10.1016/j.msec.2014.04.008
28. Berthold C, Klein R, Lühmann J, Nickel KG. Characterization of Fibres and Fibre Collectives with Common Laser Diffractometers. Part Part Syst Charact. 2000; 17:113–116. DOI: 10.1002/1521-4117(200010)17:3<113::AID-PPSC113>3.0.CO;2-Z
29. Particle Size Analysis - Laser Diffraction Methods ISO 13320 - 1:2009. n.d
30. Shi W, Song S, Zhang H. Hydrothermal synthetic strategies of inorganic semiconducting nanostructures. Chem Soc Rev. 2013; 42:5714.doi: 10.1039/c3cs60012b [PubMed: 23563082]
31. Zhang J, Nancollas GH. Interpretation of dissolution kinetics of dicalcium phosphate dihydrate. J Cryst Growth. 1992; 125:251–269. DOI: 10.1016/0022-0248(92)90339-K
32. Sadat-Shojai M, Khorasani MT, Jamshidi A. Hydrothermal processing of hydroxyapatite nanoparticles—A Taguchi experimental design approach. J Cryst Growth. 2012; 361:73–84. DOI: 10.1016/j.jcrysgro.2012.09.010
33. Sadat-Shojai M, Atai M, Nodehi A. Design of experiments (DOE) for the optimization of hydrothermal synthesis of hydroxyapatite nanoparticles. J Braz Chem Soc. 2011; 22:571–582.
34. Ito H, Oaki Y, Imai H. Selective Synthesis of Various Nanoscale Morphologies of Hydroxyapatite via an Intermediate phase. Cryst Growth Des. 2008; 8:1055–1059. DOI: 10.1021/cg070443f
35. Chen F, Zhu YJ, Wang KW, Zhao KL. Surfactant-free solvothermal synthesis of hydroxyapatite nanowire/nanotube ordered arrays with biomimetic structures. CrystEngComm. 2011; 13:1858.doi: 10.1039/c0ce00574f
36. Mathew M, Takagi S. Structures of biological minerals in dental research. J Res-Natl Inst Stand Technol. 2001; 106:1035–1044.
37. Tseng YH, Mou CY, Chan JCC. Solid-State NMR Study of the Transformation of Octacalcium Phosphate to Hydroxyapatite: A Mechanistic Model for Central Dark Line Formation. J Am Chem Soc. 2006; 128:6909–6918. DOI: 10.1021/ja060336u [PubMed: 16719471]
38. Yokoi T, Kato H, Kim IY, Kikuta K, Kamitakahara M, Kawashita M, Ohtsuki C. Formation of octacalcium phosphates with co-incorporated succinate and suberate ions. Dalton Trans. 2012; 41:2732.doi: 10.1039/c2dt11580h [PubMed: 22249371]
39. Johnsson MS, Nancollas GH. The role of brushite and octacalcium phosphate in apatite formation. Crit Rev Oral Biol Med Off Publ Am Assoc Oral Biol. 1992; 3:61–82.
40. Iijima M, Tohda H, Moriwaki Y. Growth and structure of lamellar mixed crystals of octacalcium phosphate and apatite in a model system of enamel formation. J Cryst Growth. 1992; 116:319–326. DOI: 10.1016/0022-0248(92)90639-Z
41. Iijima M, Kamemizu H, Wakamatsu N, Goto T, Doi Y, Moriwaki Y. Transition of octacalcium phosphate to hydroxyapatite in solution at pH 7.4 and 37°C. J Cryst Growth. 1997; 181:70–78. DOI: 10.1016/S0022-0248(97)00230-3
42. Wang L, Nancollas GH. Calcium Orthophosphates: Crystallization and Dissolution. Chem Rev. 2008; 108:4628–4669. DOI: 10.1021/cr0782574 [PubMed: 18816145]
43. Ito N, Kamitakahara M, Yoshimura M, Ioku K. Importance of nucleation in transformation of octacalcium phosphate to hydroxyapatite. Mater Sci Eng C. 2014; 40:121–126. DOI: 10.1016/j.msec.2014.03.034
44. Du X, Chu Y, Xing S, Dong L. Hydrothermal synthesis of calcium hydroxyapatite nanorods in the presence of PVP. J Mater Sci. 2009; 44:6273–6279. DOI: 10.1007/s10853-009-3860-6
45. Schofield PF, Knight KS, van der Houwen JAM, Valsami-Jones E. The role of hydrogen bonding in the thermal expansion and dehydration of brushite, di-calcium phosphate dihydrate. Phys Chem Miner. 2004; 31:606–624. DOI: 10.1007/s00269-004-0419-6

46. Catti M, Ferraris G, Filhol A. Hydrogen bonding in the crystalline state. CaHPO4 (monetite), P1 or P1? A novel neutron diffraction study. Acta Crystallogr B. 1977; 33:1223–1229. DOI: 10.1107/S0567740877005706
47. Zhang Y, Lu J. The transformation of single-crystal calcium phosphate ribbon-like fibres to hydroxyapatite spheres assembled from nanorods. Nanotechnology. 2008; 19:155608.doi: 10.1088/0957-4484/19/15/155608 [PubMed: 21825622]
48. Trpkovska M, Šoptrajanov B, Malkov P. FTIR reinvestigation of the spectra of synthetic brushite and its partially deuterated analogues. J Mol Struct. 1999; 480–481:661–666. DOI: 10.1016/S0022-2860(98)00923-5
49. Gashti MP, Bourquin M, Stir M, Hulliger J. Glutamic acid inducing kidney stone biomimicry by a brushite/gelatin composite. J Mater Chem B. 2013; 1:1501.doi: 10.1039/c3tb00088e
50. Fa K, Jiang T, Nalaskowski J, Miller JD. Interaction Forces between a Calcium Dioleate Sphere and Calcite/Fluorite Surfaces and Their Significance in Flotation. Langmuir. 2003; 19:10523–10530. DOI: 10.1021/la035335j
51. Mielczarski JA, Mielczarski E. Determination of Molecular Orientation and Thickness of Self-Assembled Monolayers of Oleate on Apatite by FTIR Reflection Spectroscopy. J Phys Chem. 1995; 99:3206–3217. DOI: 10.1021/j100010a035
52. Lu Y, Drelich J, Miller JD. Oleate Adsorption at an Apatite Surface Studied by Ex-Situ FTIR Internal Reflection Spectroscopy. J Colloid Interface Sci. 1998; 202:462–476. DOI: 10.1006/jcis.1998.5466
53. Bronstein LM, Huang X, Retrum J, Schmucker A, Pink M, Stein BD, Dragnea B. Influence of Iron Oleate Complex Structure on Iron Oxide Nanoparticle Formation. Chem Mater. 2007; 19:3624–3632. DOI: 10.1021/cm062948j
54. Marković S, Veselinović L, Lukić MJ, Karanović L, Bračko I, Ignjatović N, Uskoković D. Synthetical bone-like and biological hydroxyapatites: a comparative study of crystal structure and morphology. Biomed Mater. 2011; 6:045005.doi: 10.1088/1748-6041/6/4/045005 [PubMed: 21659698]
55. Davis JMG, Addison J, McINTOSH C, Miller BG, Niven K. Variations in the Carcinogenicity of Tremolite Dust Samples of Differing Morphology. Ann N Y Acad Sci. 1991; 643:473–490. DOI: 10.1111/j.1749-6632.1991.tb24497.x [PubMed: 1809161]
56. Aust AE, Cook PM, Dodson RF. Morphological and Chemical Mechanisms of Elongated Mineral Particle Toxicities. J Toxicol Environ Health Part B. 2011; 14:40–75. DOI: 10.1080/10937404.2011.556046
57. Hougaard KS, Jackson P, Jensen KA, Sloth JJ, Löschner K, Larsen EH, Birkedal RK, Vibenholt A, Boisen AMZ, Wallin H, Vogel U. Effects of prenatal exposure to surface-coated nanosized titanium dioxide (UV-Titan). A study in mice. Part Fibre Toxicol. 2010; 7:16.doi: 10.1186/1743-8977-7-16 [PubMed: 20546558]
58. Poland CA, Duffin R, Kinloch I, Maynard A, Wallace WAH, Seaton A, Stone V, Brown S, MacNee W, Donaldson K. Carbon nanotubes introduced into the abdominal cavity of mice show asbestos-like pathogenicity in a pilot study. Nat Nanotechnol. 2008; 3:423–428. DOI: 10.1038/nnano.2008.111 [PubMed: 18654567]
59. Ji Z, Wang X, Zhang H, Lin S, Meng H, Sun B, George S, Xia T, Nel AE, Zink JI. Designed Synthesis of CeO_2 Nanorods and Nanowires for Studying Toxicological Effects of High Aspect Ratio Nanomaterials. ACS Nano. 2012; 6:5366–5380. DOI: 10.1021/nn3012114 [PubMed: 22564147]
60. Zhao X, Ng S, Heng BC, Guo J, Ma L, Tan TTY, Ng KW, Loo SCJ. Cytotoxicity of hydroxyapatite nanoparticles is shape and cell dependent. Arch Toxicol. 2013; 87:1037–1052. DOI: 10.1007/s00204-012-0827-1 [PubMed: 22415765]
61. Xu Z, Liu C, Wei J, Sun J. Effects of four types of hydroxyapatite nanoparticles with different nanocrystal morphologies and sizes on apoptosis in rat osteoblasts: Effects of hydroxyapatite nanoparticles on rat osteoblasts. J Appl Toxicol. 2012; 32:429–435. DOI: 10.1002/jat.1745 [PubMed: 22162110]

62. Yuan Y, Liu C, Qian J, Wang J, Zhang Y. Size-mediated cytotoxicity and apoptosis of hydroxyapatite nanoparticles in human hepatoma HepG2 cells. Biomaterials. 2010; 31:730–740. DOI: 10.1016/j.biomaterials.2009.09.088 [PubMed: 19836072]

63. Zhao X, Ong KJ, Ede JD, Stafford JL, Ng KW, Goss GG, Loo SCJ. Evaluating the Toxicity of Hydroxyapatite Nanoparticles in Catfish Cells and Zebrafish Embryos. Small. 2013; 9:1734–1741. DOI: 10.1002/smll.201200639 [PubMed: 22887936]

64. Scheel J, Weimans S, Thiemann A, Heisler E, Hermann M. Exposure of the murine RAW 264.7 macrophage cell line to hydroxyapatite dispersions of various composition and morphology: Assessment of cytotoxicity, activation and stress response. Toxicol In Vitro. 2009; 23:531–538. DOI: 10.1016/j.tiv.2009.01.007 [PubMed: 19444930]

65. Albrecht C, Scherbart AM, van Berlo D, Braunbarth CM, Schins RPF, Scheel J. Evaluation of cytotoxic effects and oxidative stress with hydroxyapatite dispersions of different physicochemical properties in rat NR8383 cells and primary macrophages. Toxicol In Vitro. 2009; 23:520–530. DOI: 10.1016/j.tiv.2009.01.005 [PubMed: 19444929]

66. Uskoković V, Desai TA. Phase composition control of calcium phosphate nanoparticles for tunable drug delivery kinetics and treatment of osteomyelitis. I. Preparation and drug release. J Biomed Mater Res A. 2013; 101A:1416–1426. DOI: 10.1002/jbm.a.34426 [PubMed: 23115118]

67. Uskoković V, Batarni SS, Schweicher J, King A, Desai TA. Effect of Calcium Phosphate Particle Shape and Size on Their Antibacterial and Osteogenic Activity in the Delivery of Antibiotics in Vitro. ACS Appl Mater Interfaces. 2013; 5:2422–2431. DOI: 10.1021/am4000694 [PubMed: 23484624]

Appendix A. Supplementary data

Tables showing crystallite sizes of samples 1 – 8; SEM images accompanied with particle size distribution from laser diffraction; optical microscopy images of precursors and samples; and R markdown file showing the code for decomposition of mixed distributions applied on XRD data and size distribution data.

Highlights

- novel hydrothermal synthesis of HA nanowires
- controlled synthesis of 1D and 2D morphologies
- high level of biocompatibility of nanowires

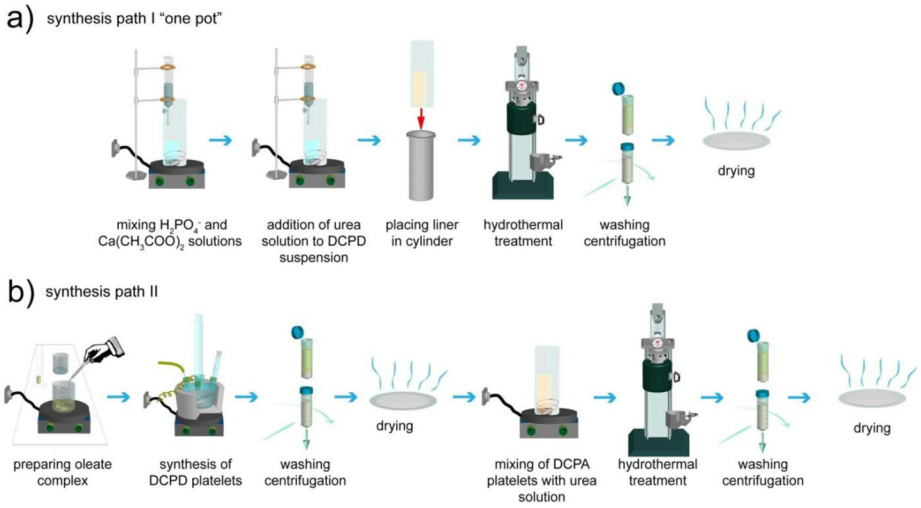

Figure 1.

The sketch of "one-pot" route for the synthesis of 1D HAstructures (a), and the two-stage 1D HA synthesis route via DCP platelets (b).

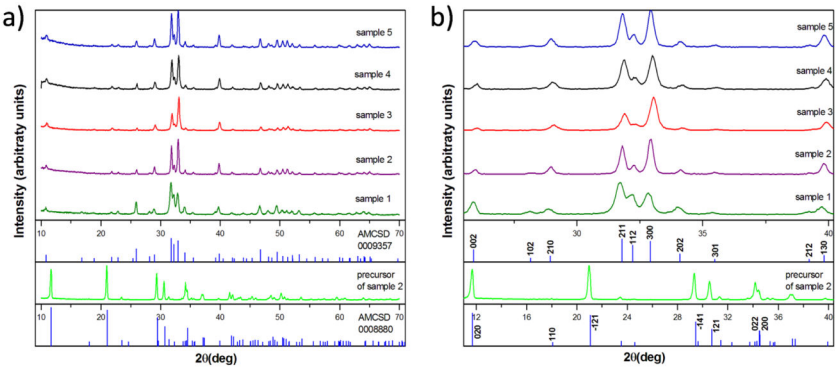

Figure 2.

XRD patterns of precursor for samples 1 and 2 and for samples from 1 to 5 within the whole 2Θ measurement range (a) and with a zoom on a selected interval (b). The diffractograms are compared to the reflections of the reference AMCSD code 0008880 and code 0009357 corresponding to DCPD (brushite) and pure HA, respectively.

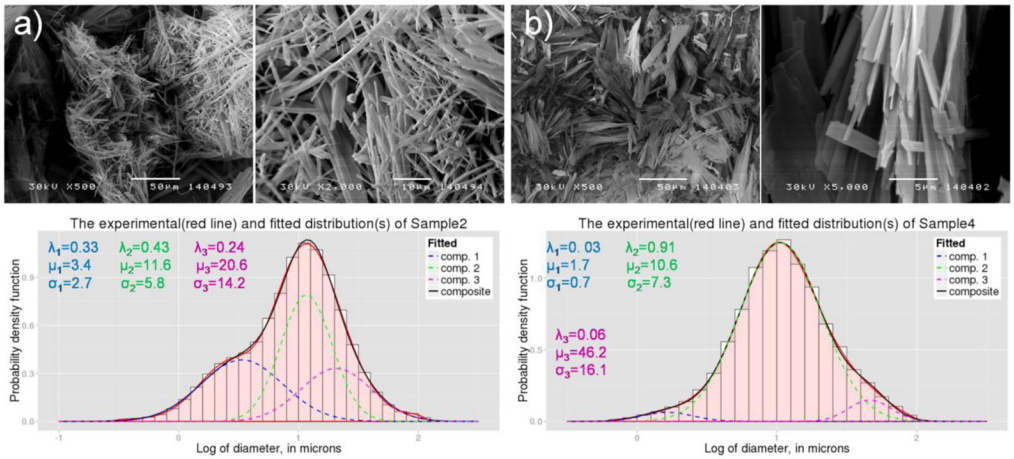

Figure 3.

SEM images of 1D HA along with the particle size distributions for Samples 2 (a) and 4 (b), including the mixing proportion and other parameters for the convoluted components of the distributions. The μ-s and σ-s are given in microns. Scale bars are a) 50 and 10 μm and b) 50 and 5 μm respectively.

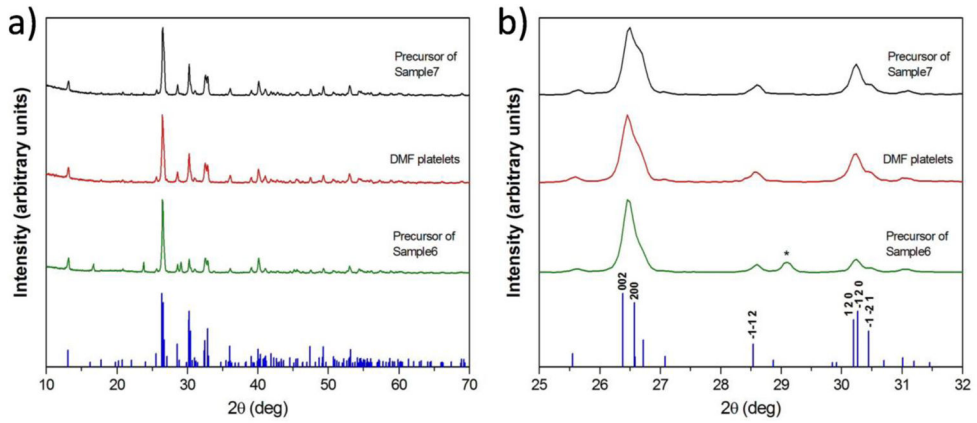

Figure 4.

XRD patterns of the precursors for the hydrothermal synthesis of HA following the second, two-step route (a) for the whole 2Θ measurement range and (b) with a zoom on a selected interval. The star (*) denotes an unidentified impurity in sample 6 (b). The patterns are compared with the reference cards for brushite – DCPD code no. 0008880 [45] and monetite – DCPA code no. 0009584 [46].

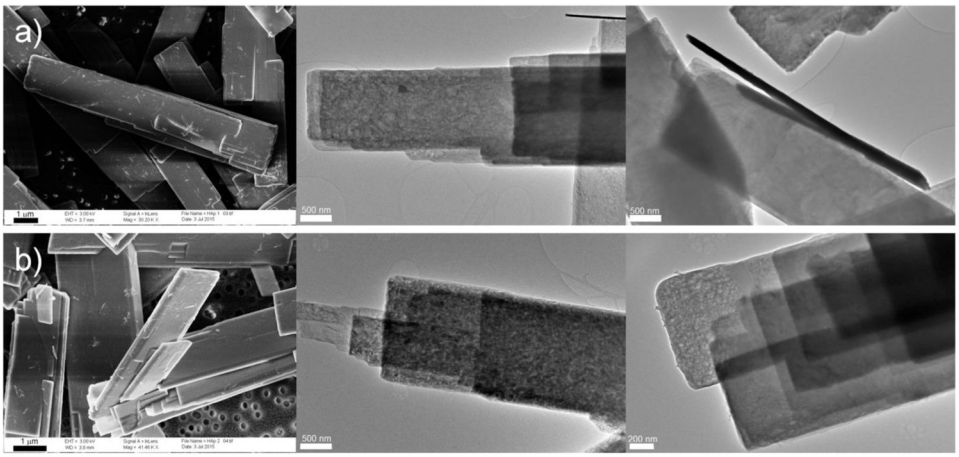

Figure 5.

SEM and TEM images of platelets as precursors for the hydrothermal synthesis of Samples 6 (a) (scale bars 1 µm and 500 nm) and 7 (b) (scale bars 1 µm, 500 nm and 200 nm), revealing laminated microstructure.

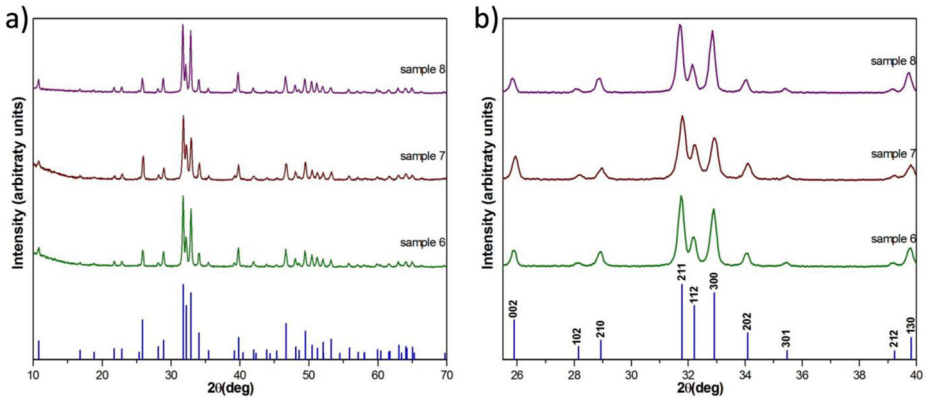

Figure 6.

XRD patterns of Samples 6, 7 and 8 compared to the reference AMCSD code 0009357 corresponding to pure HA.

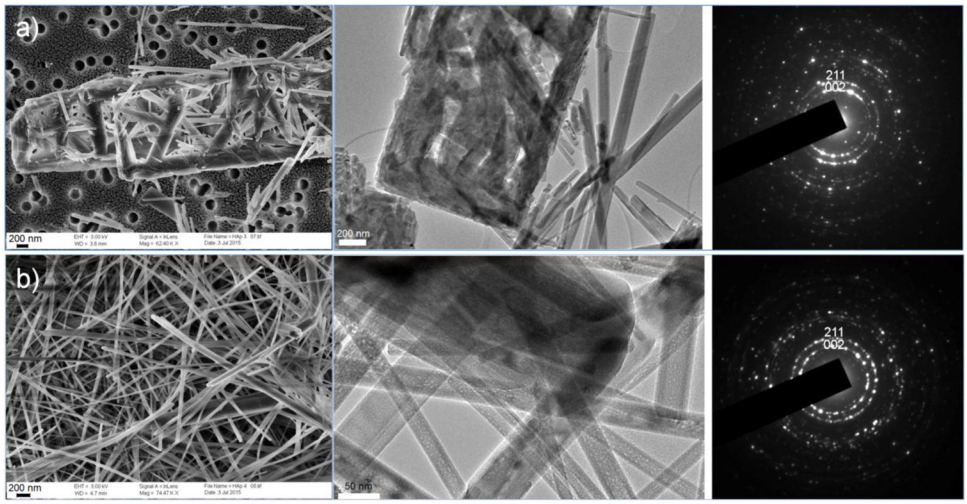

Figure 7.

FE-SEM, TEM images and electron diffractions of Samples 6 (a) (scale bars 200 nm) and 7 (b) (scale bars 200 and 50 nm). SAED patterns are identified as HA reflections.

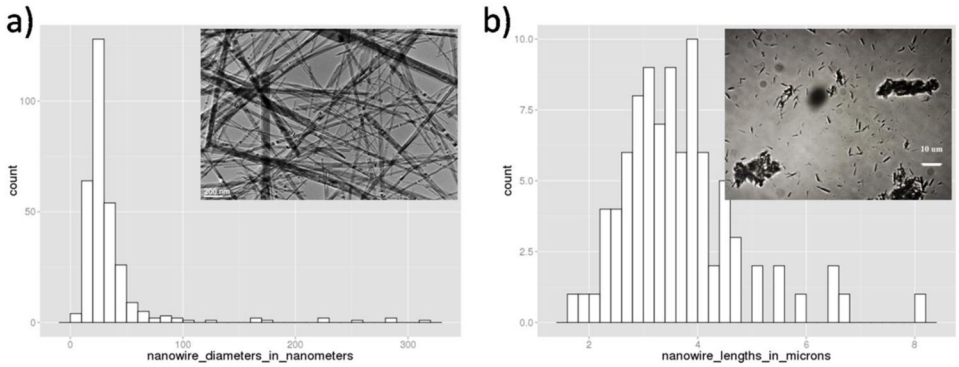

Figure 8.

Distribution of the diameters and lengths of HA nanowires comprising Sample 7, resulting from the comparative analysis of several TEM and optical microscopy images. The mean diameter and length of HA nanowires are 37 nm and 3.7 microns respecively.

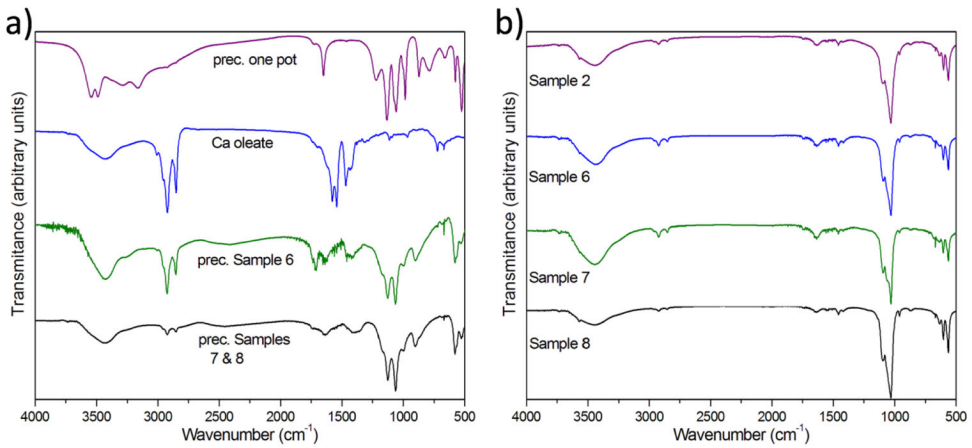

Figure 9.

FTIR spectra of precursors for the hydrothermal synthesis of HA (a) and of the products (Samples 2, 6, 7, 8) (b).

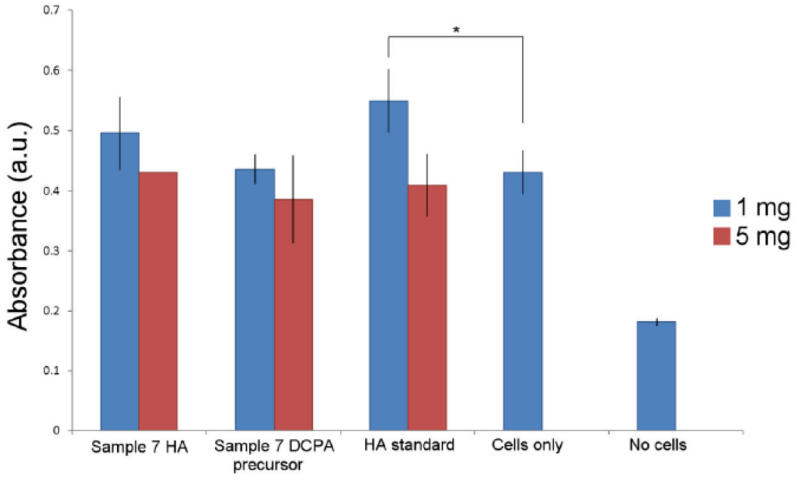

Figure 10.

MTT assay absorbance indicative of the viability ofosteoblastic MC3T3-E1 cells incubated with various calcium phosphate powders at the concentrations of 0.5 and 2.6 mg/cm^2 (1 and 5 mg per well and per ml of media in the standard 24-well plate, respectively). All the data are represented as averages of three independent cell/particle analyses. Error bars represent the standard deviation (for Sample 7 HA at 5 mg/ml it is invisible to the eye). Data points significantly different from the “cell only” control ($p < 0.05$) are marked with an asterisk.

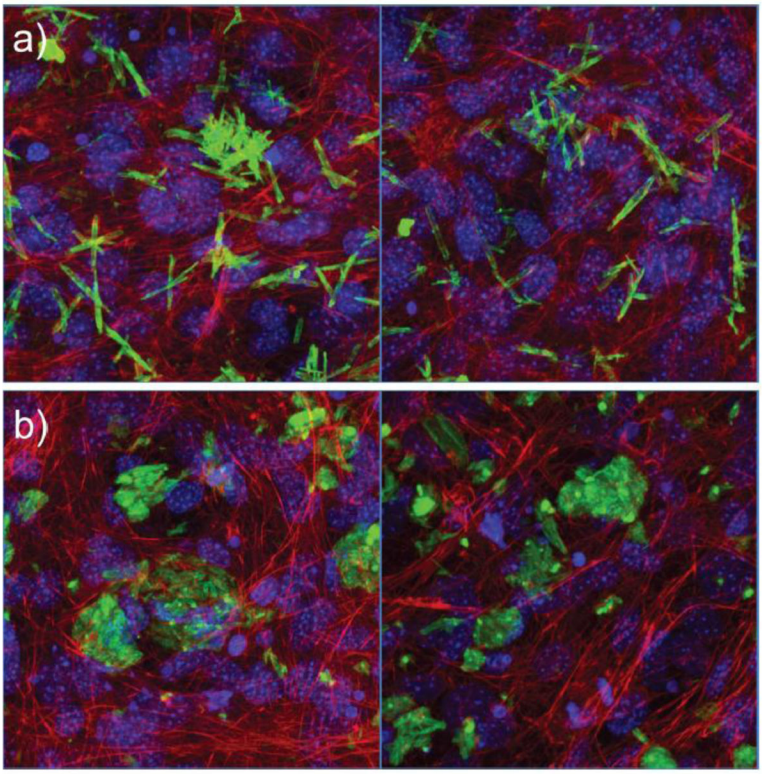

Figure 11.

Confocal optical micrographs of MC3T3-E1 cells incubated either with identical amounts (5 mg/well) of Sample 7 HA particles (a) or Sample 7 precursor DCPA particles (b) and culturedfor 7 days. Green – calcium phosphate particles; blue – MC3T3-E1 cell nuclei; red – f-actin cytoskeletal microfilaments.

Table 1

The hydrothermal synthesis parameters

	Sample1	Sample2	Sample3	Sample4	Sample5
Ca/P	1.2	1.2	1	1	1
PVP (g/l)	none	none	None	2	none
Hydrothermal reaction time (h)	20	96	20	20	48
pH after the hydrothermal reaction	9	10	9–10	9	9–10

Table 2

Parameters describing the synthesis of 1D HA structures in the two-stage process

		Sample6	Sample7	Sample8
Precursor synthesis	Ca/P	0.5	0.5	0.5
	DMF	none	100 ml	100 ml
	Drying	yes	yes	no
Hydrothermal synthesis	Time (h)	72	72	72
	pH after the hydrothermal reaction	10	10	10